Sensors & Actuators: B. Chemical 319 (2020) 128158

Contents lists available at ScienceDirect

Sensors and Actuators B: Chemical

journal homepage: www.elsevier.com/locate/snb

Fast detection of alcohols by novel sea cucumber-like indium tungsten oxide

Chong Wang[a], Yiqun Zhang[a], Xiaoying Sun[a,*], Yanfeng Sun[b], Fangmeng Liu[b], Xu Yan[b], Chenguang Wang[b], Peng Sun[b], Geyu Lu[b,*]

[a] College of Communication Engineering, Jilin University, Changchun, 130022, Jilin, China
[b] State Key Laboratory on Integrated Optoelectronics, College of Electronic Science and Engineering, Jilin University, Changchun, 130012, Jilin, China

ARTICLE INFO

Keywords:
Gas sensor
alcohols
oxide semiconductor
sea cucumber nanostructure

ABSTRACT

Novel sea cucumber-like indium tungsten oxide is synthesized by a one-step solvothermal method without surfactant. Interestingly, sensors based on this kind of indium tungsten oxide achieve the detection of some target gases with certain characteristics, which has been rarely reported until now. In this paper, response of the sensor to 200 ppm of methanol, ethanol, n-propanol, n-butanol, n-pentanol and n-hexanol is 11.4, 20.5, 22.3, 23.7, 23.2 and 17.1, respectively, which is significantly higher than to other gases, indicating that the cucumber-like indium tungsten oxide is especially sensitive to straight-chain alcohols with -OH function group at the end of the chain. In addition, the response time is 2 s, 2 s, 2 s, 2 s, 2 s and 17 s, respectively, which facilitates rapid detection in real application. The sea cucumber-like nanostructures can be only formed under the condition that molar ratio of $In(NO_3)_3{\cdot}4.5H_2O$ to $Na_2WO_4{\cdot}2H_2O$ is 2:1 and volume ratio of alcohol to deionized water is 3:2. The sea cucumber-like nanostructures possess nanothorns vertically distributed on the surface of the main nanoellipsoid. The long axis of the nanoellipsoid is about 800 nm, and the short axis is about 270 nm. This is a kind of non-stoichiometric ratio compound consisting of indium, tungsten and oxide elements speculated by XRD, XPS and EDX characterizations. The field emission scanning electron microscopy characterization reveals the growth process and the morphology evolution of the material.

1. Introduction

Construction of hierarchical nanostrcutures has been found to be effective to enhance the physical and chemical properties of the functional materials [1]. At present, this method is widely used in fuel cells [2], photocatalysis [3] and gas sensors [4], etc. In the field of gas sensors, sensing materials with hierarchical nanostructures is difficult to aggregate, providing well-aligned porous structures to accomplish high response and fast response speed when detecting target gas [4]. For this reason, it is possible for gas sensor to exhibit high sensing performance by micro-nanostructure design. A variety of hierarchical nanostructures have been reported before, such as nanoleaf [5], nanosphere [6], nanoflower [7], etc. While, novel nanostructures are still desired to show more remarkable performances when detecting gases.

Gas sensors based on metal oxide semiconductor (MOS) play a significant role in the detection of toxic gases attributed to the low cost, small size, high sensitivity and easy preparation. Up to now, binary oxide semiconductors have always been the focus of research. Numerous reports introduced the investigations on SnO_2 [8–9], ZnO [10–11], WO_3 [12–13], In_2O_3 [14–15], NiO [16–17] and CuO [18–19]. However, there is less research on ternary oxide semiconductors. Recently, the ternary oxide semiconductors attract growing attention due to their potential application in the field of gas sensors. Xu et al. synthesized Zn_2SnO_4 microspheres to detect H_2S, Li et al. synthesized ZnO/$ZnCo_2O_4$ hierarchical structures for TEA detection [20–21]. Lupan et al. fabricated enhanced hydrogen gas sensors using $Zn_xCu_{1-x}O_y$ nanocrystals as sensing material [22]. It is found that most of the investigations about ternary oxide semiconductors are spinel structure and inverse spinel structure. There is less research on other types of ternary oxides. Exploring novel new ternary oxide semiconductor materials has important scientific and practical significance for designing high-performance gas sensors.

House painting, automobile exhaust, petroleum production, and many other human activities (straw burning, cooking, etc.) emitted large amounts of volatile organic compounds (VOCs) indoors and outdoors [23]. The VOCs usually include alcohols, ketones, benzenes, etc. Excessive inhalation of the VOCs could cause headache, blindness, or other long-term effect on human health (eg: cancer) [24–27]. The VOCs monitoring is of great significance for safeguarding human health and preventing environmental pollution. Many researchers devoted

* Corresponding author.
E-mail address: lugy@jlu.edu.cn (L. Geyu).

https://doi.org/10.1016/j.snb.2020.128158
Received 31 December 2019; Received in revised form 6 April 2020; Accepted 16 April 2020
Available online 21 April 2020

themselves to the design of gas sensors for the detection of VOCs, such as ethanol gas sensor [28–29], acetone gas sensor [30–31], formaldehyde gas sensor [32–33], toluene gas sensor [34–35]. Most of the investigations focused on the detection of one target gas, but some methods were also proposed to detect two gases. For instance, Lee et al. tried to detect xylene and toluene by adjusting the operating temperature of the sensor based on Nb-doped NiO hollow spheres [36], Kim et al. realized toluene and benzene detection by loading Pt and Pd nanoparticles on ZnO nanowires [37], Lupan et al. changed the sensing properties from the ethanol vapour (pure copper oxide) to hydrogen gas (zinc-doped copper oxide) by doping with Zn in copper oxide[22]. Although the detection of two gases can be achieved, modification of the sensing material or adjusting of operating temperature is still required. However, there is almost no literature about gas sensors for detection of some target gases with certain characteristics.

In this paper, one-pot solvothermal method and subsequent annealing treatment are employed to synthesize non-stoichiometric ratio indium tungsten oxide with sea cucumber-like nanostructure. To the best of our knowledge, this special nanostructure has not been synthesized as sensing material before. The sea cucumber-like nanostructures-based gas sensor shows remarkable sensing performance to alcohols, especially to methanol, ethanol, n-propanol, n-butanol, n-pentanol and n-hexanol. This is the first time that indium tungsten oxide is found to be sensitive to straight-chain alcohols with -OH function group at the end of the chain. The possible mechanism for this sensing behavior is proposed here. High response and fast response-recovery characteristic prove this hierarchical nanostructure is a kind of promising sensing material for gas sensor.

2. Experiment section

2.1. Synthesis of sensing material

All the stirring operations were accomplished by a magnetic stirrer under room temperature. In the typical synthesis, 10 ml of deionized water and 15 ml of ethanol were mixed by stirring with 1000 rpm for 5 minutes. 1.5 mmol $Na_2WO_4{\cdot}2H_2O$ was dissolved into the mixed solution, the solution became clear after stirring with 1000 rpm for 10 minutes. Then, 1.5 mmol $In(NO_3)_3{\cdot}4.5H_2O$ was added into this clear solution, the solution turned white almost simultaneously. After stirring with 1000 rpm for another 10 minutes, the above turbid fluid was transformed into the lining of Teflon-lined autoclave. The lining is made of polytetrafluoroethylene with volume of 45 ml. Tighten the lid of the autoclave with a wrench to guarantee the airtight of the lining. The autoclave was then put into an oven which was set to 200 ˚C for 24 h. When the autoclave cooled down to room temperature, open the autoclave to remove the lining. Supernatant in the lining was discarded and white precipitates deposited at the bottom were collected. Then, the collected precipitates were placed in 50 ml centrifuge tube filled with 40 ml deionized water. The centrifuge tube was put into a centrifuge which was set to10000 rpm for 10 minutes. Followed by ethanol after deionized water. After being washed 7 times in total, the precipitates were poured out into a petri dish and dried in an oven at 80 ˚C for 24 h. Finally, the dried precipitates were heated at 500 ˚C for 2 h in air atmosphere with a heating rate of 2 ˚C/min to get the sensing material.

2.2. Material characterization

X-ray power diffraction (XRD) analysis was conducted on a Rigaku D/max-2500 X-ray diffractometer with Cu Ka1 radiation (l ¼ 1.54056 A) in the range of 20 ˚-70 ˚. The morphology and nanostructure of the material was examined by field-emission scanning electron microscopy (FESEM, JEOL JSM-7500 F, operated at an acceleration voltage of 15 kV). Transmission electron microscopy (TEM) and selected-area electron diffraction (SAED) were obtained on a JEOL JEM-2100 microscope operated at 200 kV. Differential scanning calorimetric (DSC) measurements were also carried out using a NETZSCH STA 449F3 simultaneous thermogravimetric analyzer under air atmosphere in the temperature range from 30 to 800 ˚C with a heating rate of 10 ˚C / min. X-ray photoelectron spectroscopy (XPS).

2.3. Fabrication and measurement of sensor

The synthesized indium tungsten oxide powders were used as sensing material to fabricate a sensor. 20 mg of the sensing material was mixed with two drops of deionized water to form a homogeneous paste. The paste was coated onto the surface of an alumina tube with a small brush. Two gold electrodes were installed on the alumina tube, each gold electrode connected with two Pt wires. The alumina tube was coated with the small brush for several times until the gold electrodes were not visible. Then, the alumina tube was put under infrared light for 10 min. Then, the alumina tube was sintered at 300 ℃ for 2 h in a muffle furnace to evaporate the water and impurities introduced in the sensing material during the coating process. Finally, the alumina tube was soldered to the pedestal by electric welding, a Ni–Cr alloy coil inserted in the internal of the tube to provide operating temperature. In this paper, the response of the sensor is defined as S = Ra/Rg, Ra and Rg represent the resistances of the sensor in air and target gas. The response time and recovery time represent the time of the sensor takes to achieve 90% of the total resistance change. The testing schematic diagram is given in Fig. S1. The detailed testing process was described in previous work [38].

3. Results and discussion

3.1. Characterizations of indium tungsten oxide

XRD patterns of the sample are displayed in the Supporting Information (Fig. S2). XPS characterization was performed in order to figure out the element and composition of the sample, the results are displayed in Fig. 1. In $3d_{5/2}$ and In $3d_{3/2}$ XPS peaks are found located at binding energies of 445 and 452.65 eV (Fig. 1 (a)), excluding the existence of metallic indium located at 443.6 eV [39]. Compared with the reported literature, the indium element contained in the sample is mainly In $^{3+}$ [40]. W $4f_{7/2}$ and W $4f_{5/2}$ appears at 36.4 and 38.4 eV (Fig. 1(b)), respectively, representing the valence state for tungsten is W^{6+} [41]. The O 1s peak is decomposed into three fitted peaks in Fig. 1 (c), which is attributed to the lattice oxygen species (Ol), oxygen ions in oxygen deficient regions (Ov), and chemisorbed oxygen species (Oc) (O_2^-, O^- and OH^- etc) from lower binding energy to higher binding [42]. The relative percentage of O species is given in Fig. 1(d1). The content of Ol, Ov and Oc is 50.5%, 34.2%, 15.3%, respectively. As reported, the surface defects has ability to attract adsorbed oxygen to enhance the gas sensing performance [43]. The high Ov content here plays as activate centers for the adsorption of oxygen, inducing high gas response. As the atom content listed in Fig. 1(d2), the molar ratio of In, W, O is 1: 1.27: 6.69. Strong signal peaks of indium, tungsten, oxide elements are also observed by EDX characterization in Fig. S3(a). The elements distribution of Fig. S3(b) is shown in Fig. S3(c)-(e). The molar ratio of In, W, O is 1(± 0.32): 1.07(± 0.18): 4.96(± 0.63) by the EDX results, which is consistent with the XPS results.

The morphologies and nanostructures of the samples obtained at different reaction time were observed by FESEM. Initially, the sample contained numerous agglomerated nanoparticles can be observed with diameter of 30 - 40 nm when the reaction time was only 1 h (Fig. 2(a)). As the reaction time increased to 3 h, some nanoellipsoids began to appear as marked in Fig. 2(b). Prolonging the reaction time to 6 h could result in the formation of numerous nanoellipsoids with ~800 nm in long axis and ~270 nm in short axis, the agglomerated nanoparticles disappeared. It could be observed that some nanothorns vertically distributed on the surface of the main nanoellipsoid, as shown in

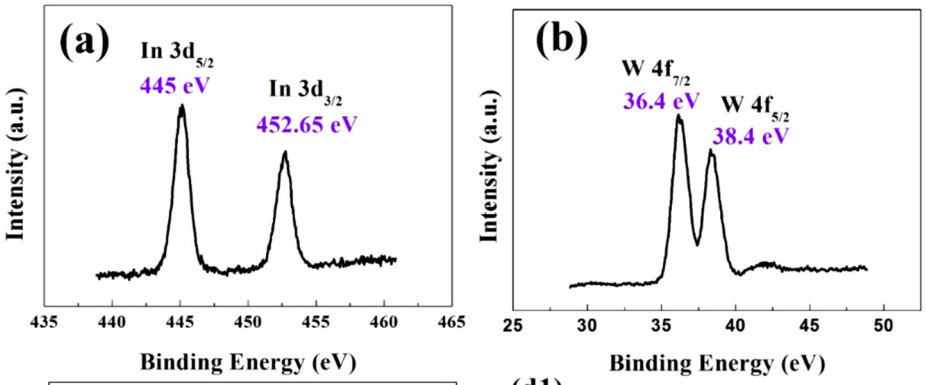

(d1)

Oxygen Species	Content (%)
Ol	50.5
Oc	15.3
Ov	34.2

(d2)

Atom	Atom Content (%)
In	2.67
W	3.41
O	17.85
C	76.07

Fig. 1. XPS spectra of (a) In 3d, (b) W 4f, (c) O 1s. (d1) Fitting Results of O 1s. (d2) Atom content of the sample.

Fig. 2(c). The size of the nanoellipsoids remained unchanged as the reaction time was extended to 24 h, but both the number and the size of the nanorods increased respectively. All the nanoparticles in the initial stage developed into fully sea-cucumber like nanostructures after 24 h solvothermal reaction (Fig. 2(d)).

The schematic representation of the morphology evolution in combination with SEM results is given in Fig. 2(e). The formation mechanism could be concluded to a three-step development procedure. Step 1: nucleation process. In this stage, a great number of nanoparticles with tens of nanometers formed which were not stable due to the high surface energy. These nanoparticles had tendency to further aggregate as intermediates. Step 2: aggregation to primary nanostructures. The neighboring nanoparticle intermediates aggregated to nanoellipsoids via a self-assemble process in order to reduce the surface energy. In this stage, primary nanoellipsoids with coarse surface were formed, which provided support for the secondary crystal growth. Step 3: secondary-nanostructures growth. The reagents concentration and volume ratio of alcohol to deionized water were key factors that determined the secondary-nanostructures growth in this experiment. As the previous research reported [44], only nanoellipsoids could be synthesized when having low reactants concentration with deionized water as solvent. However, some nanothorns began to grow on the surface of the primary nanoellipsoid-like nanostructures when the reactant concentration was high enough with adjusting the solvent ratio in this experiment. As the high chemical potential of the system promoted the acceleration of the nucleation and resulted in the secondary growth. During this stage, the nanothorns gradually formed a vertical distribution on the coarse surface through an oriented attachment. As a result, fully sea-cucumber like nanostructures formed at last through the nucleation process, aggregation to primary nanostructures process and secondary-nanostructures growth process.

The TEM images of the samples annealed at 500 °C are shown in Fig. 2(f), indicating high yield of the sea cucumber nanostructures. The SAED pattern of the nanothorn marked in Fig. 2(g) is given in Fig. 2(h), confirming the nanothorn is single crystalline in nature. The EDX elemental scanning images of the sea cucumber nanostructure are presented in Fig. 2(i)-(l), the different colors represent In, W, and O elements. The signal of In is weaker than W and O, further revealing that the content of In is lower than W and O, which has been proved by XPS result.

Annealing process was performed to remove moister and organics adsorbed on the surface of the sample to stabilize the properties of the sensing materials. Thermogravimetric (TG) analysis was executed from 30 °C to 800 °C with a rate of 10 °C/min to choose the suitable annealing temperature. According to the TG curve in Fig. 3, the first weight loose is about 0.8% from 30-170 °C which could be attributed to the removing of physisorbed water on the surface of the sample. Then the weight of the sample gradually decreases about 3% as further increasing the annealing temperature from 170-500 °C. However, there is no phase transition by analyzing the XRD results, thus, we assume the pyrolysis of the organics adsorbed on the surface of the sample might be the reason for this part of weight loose. Then, there is only slight fluctuations in weight above 500 °C. Based on the thermal behavior of the sample according to the TG curve, the products were annealed at 500 °C and 600 °C respectively. The morphologies of the samples obtained after solvothermal reaction as well as annealing at 500 °C and 600 °C were observed under the same magnification and presented in Fig. 3. Before annealing, we could observe the irregular distribution of the nanothorns on the pretty rough surface. There was no obvious change on the morphology under the treatment of 500 °C except the surface of the nanoellipsoid became a little smoother. However, the morphology was destroyed when annealed at 600 °C: significant shrinkage of the size and disappearance of the nanothorns. The nanothorns collapsed to nanoparticles caused by the excessive annealing temperature. The nitrogen adsorption and desorption isotherm plots are given in Fig. 4, the BET surface area of the samples annealed at 500 °C and 600 °C is calculated to be 10.73 and 9.72 $m^2 g^{-1}$ respectively. Annealing at 600 °C causes a slight decrease in BET surface area, which is not conducive to sensitivity improvement. By comparison, 500 °C is more suitable than 600 °C for keeping the morphology unchanged to

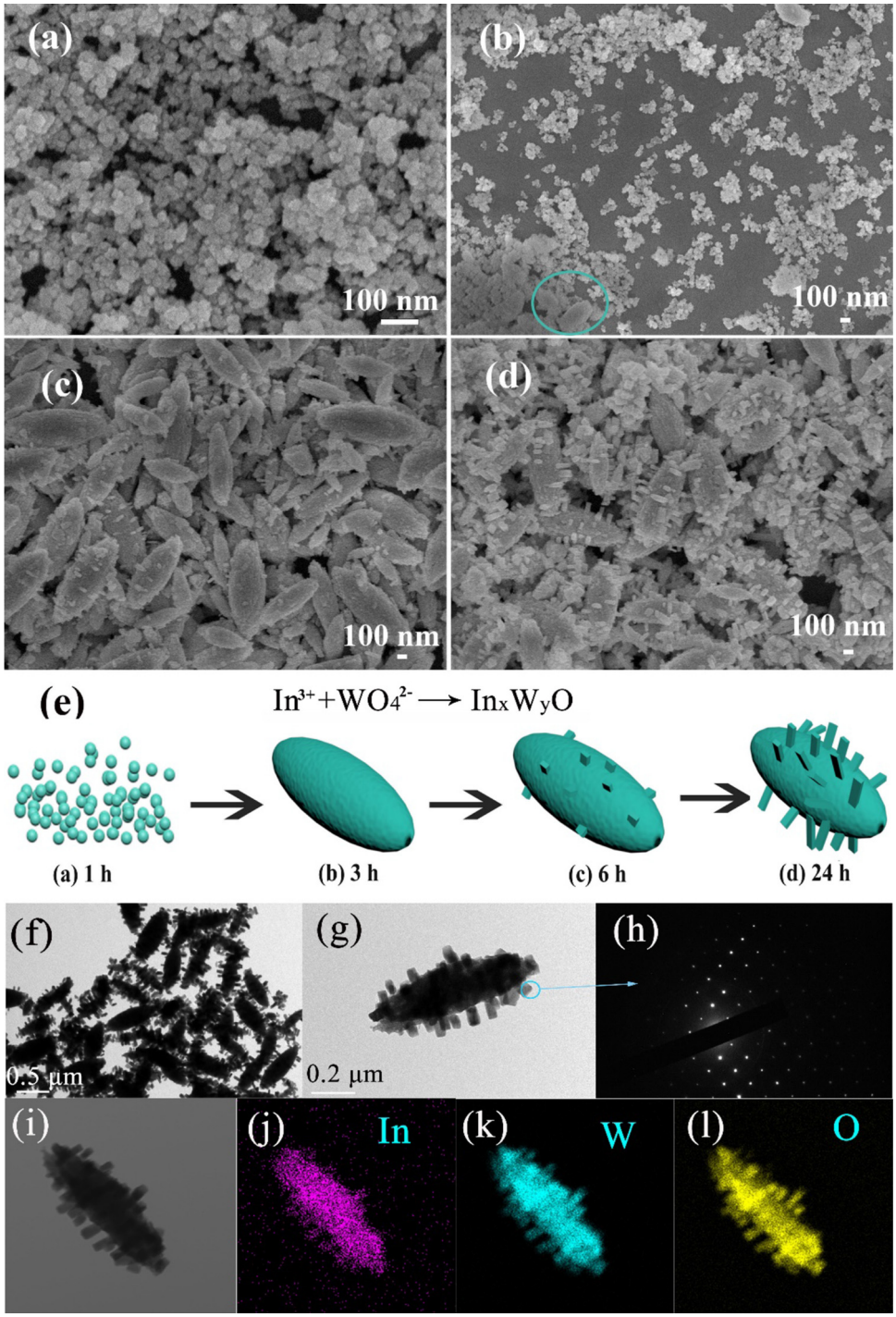

Fig. 2. Typical SEM images of the samples synthesized at 180 °C for (a) 1 h, (b) 3 h, (c) 6 h, (d) 24 h. (e) Schematic representation of the morphology evolution leading to the formation of sea-cucumber nanostructure. (f) Typical TEM images of the samples, (h) the SAED pattern of the nanothorn marked in (g), (i)-(l) EDX elemental maps of an individual sea cucumber nanostructure.

exhibit superior sensing performance.

3.2. Gas sensing properties

After annealing at 500 °C, the sea-cucumber nanostructures-based gas sensor was fabricated to investigate the sensing performance. The testing environment was under a relative humidity of 30-50 % at 23-25 °C. Responses of the sensor to 200 ppm methanol, ethanol, n-propanol, n-butanol, n-pentanol, n-hexanol were tested at different operating temperatures ranging from 300 °C to 400 °C, the results are given in Fig. 5(a). According to the curves, the responses increase from 300 °C to 325 °C and reach the maximum at 325 °C for all the tested gases. The responses trend to decrease gradually with increasing the operating temperature from 325 °C to 400 °C. Thus, 325 °C is regarded as the optimal operating temperature for the sea-cucumber nanostructures-based gas sensor to detect methanol, ethanol, *etc*. There is a widely accepted explanation for the "increase first and decrease later" response [45]. The current sensitive mechanism used to explain oxide semiconductors is the change of the resistance caused by the reaction of gas molecules on the surface of the material [4]. The moderate high

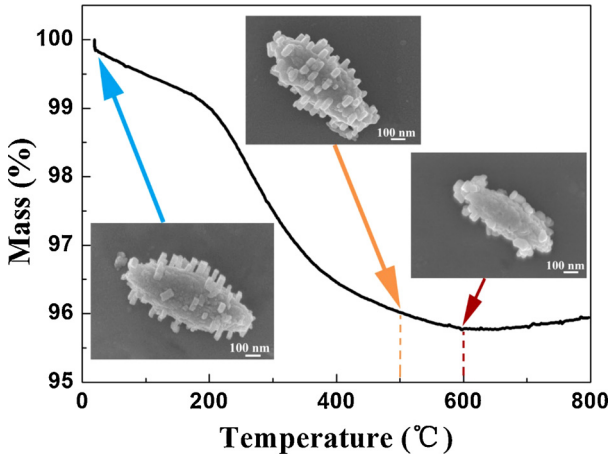

Fig. 3. TG curve and morphologies of the samples before and annealed at 500 °C and 600 °C.

operating temperature provides more energy, resulting in the stronger reaction happened on the surface of the material. While, the desorption speed of the gas is too fast to complete the reaction when the operating temperature is too high [46–48]. Thus, the balance between adsorption and desorption establishes at the optimal operating temperature and induces the highest response.

Another interesting phenomenon can be observed from the curves is the relationship between gas response and the carbon atom numbers (CAN) of the alcohols. The methanol, ethanol, n-propanol, n-butanol, n-pentanol, n-hexanol belongs to straight chain alcohol gas molecules with various CAN ranging from 1 to 6. The responses to the above gases at 325 °C with concentration of 200 ppm are obtained from Fig. 5(a) and concluded in Fig. 5(b), which shows a volcano-shaped curve. The gas response is 11.40 when the carbon number is 1. As increasing the CAN from 2 to 4, the response is 20.46, 22.34, 23.65, respectively. Then, the gas response decreases with increasing the CAN from 5 to 6. Gas response to ethanol, n-propanol, n-butanol, n-pentanol are around 22 as marked by the red circle in Fig. 5(b). To discuss the effect of -OH position on the gas response, sensing performance to isopropanol ($CH_3CHOHCH_3$) was studied. As a result, the gas response to 200 ppm of isopropanol is only 4 at 325 °C. As is known, -OH is an electron-withdrawing group, $-CH_3$ is an electron-donating group. The $CH_3CHOHCH_3$ has two $-CH_3$ groups, but the $CH_3CH_2CH_2OH$ has only one $-CH_3$ group. More $-CH_3$ groups induce stronger C-OH bond energy. Based on this theory, it is harder to break the C-OH bond in $CH_3CHOHCH_3$. As a result, the sensor has higher response to $CH_3CH_2CH_2OH$ compared with $CH_3CHOHCH_3$. With increasing the CAN, longer distance between -OH and $-CH_3$ weaken the C-OH bond energy. Therefore, the gas response increases with increasing the CAN. Therefore, the CAN is a dominant parameter that affects the response. While, the viscosity of the gas molecule participates in the impact on the gas response with further increasing the CAN. At 20 °C, the liquid viscosity of methanol, ethanol, n-propanol, n-butanol, n-pentanol, n-hexanol is 0.58, 1.074, 2.256, 2.95, 3.31, 5.2 (mPa·s) respectively. Obviously, the liquid viscosity increases with increasing the CAN. The n-hexanol possesses the maximum viscosity among them. There are enough reasons to speculate that the viscosities of the corresponding gas molecules have the similar trends: increase with increasing the CAN. Therefore, the gas response of the sensor to n-hexanol drops sharply as observed from Fig. 5(b). From the above analysis results, it is considered that the gas response of the sensor is sensitive to the CAN and the viscosity of the gas molecule.

Represent real-time response curves of the sensor to methanol with concentrations ranging from 1 ppm to 200 ppm are shown in Fig. S4. For all the target gases, the corresponding function relationship between gas response and concentration is given in Fig. 6, the inset in Fig. 6 is the enlarge image of the responses at low gas concentration from 1 ppm to 10 ppm. From the inset, it is observed that the gas responses to n-pentanol and n-hexanol are lower than to methanol, ethanol, n-propanol, n-butanol when the gas concentration is 1 ppm. We deduce that only small amount of gases could adsorb onto the surface of the material due to high gas viscosity at low concentration, inducing low gas responses. The gas response of the sensor is more sensitive to the CAN as the concentration increases. Over a wide range of concentrations, the sensor exhibits higher gas responses to ethanol, n-propanol, n-butanol, n-pentanol than to methanol and n-hexanol.

To get the detailed information of the sensing characteristics, real-time resistance curves of the sensor to 200 ppm methanol, ethanol, n-propanol, n-butanol, n-pentanol, n-hexanol are presented in Fig. 7. The testing environment was under a relative humidity of 30-50 % at 23-25 °C. For methanol, ethanol, n-propanol, n-butanol, the sensor shows rapid response characteristic. The recovery speed is not comparable to the response speed, but the resistance can still recover to its original value. For n-pentanol and n-hexanol (blue and purple curves), the sensor needs more time to complete the recovery process, in addition, it is harder to recover to the initial resistance value. We deduce that the recovery process is affected by the viscosity of gas molecule. High viscosity prevents the desorption of the target gas during the recovery process, consequently, the recovery process of the senor for detecting n-hexanol is the hardest compared with other gases. The resistance decreases immediately once exposed to alcohols, the change of the resistance is almost instantaneous. According to the definition, the response time and recovery time for methanol, ethanol, n-propanol, n-butanol, n-pentanol, n-hexanol are 2 s/16 s, 2 s/19 s, 2 s/33 s, 2 s/36 s, 2 s/66 s, 17 s/103 s. The sensor exhibits fast detection to alcohols. However, the recovery time becomes longer as the CAN increases. We

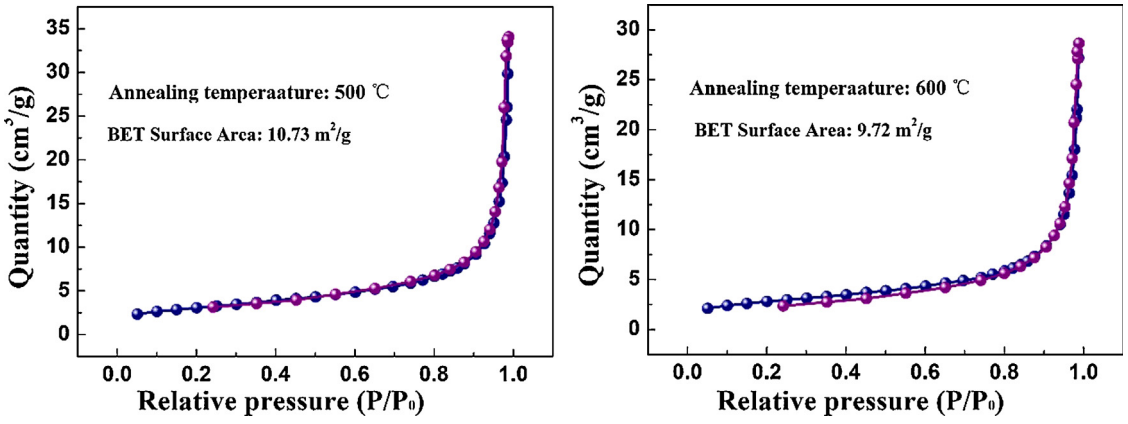

Fig. 4. Nitrogen gas adsorption-desorption isotherns of the samples annealed at 500 °C and 600 °C.

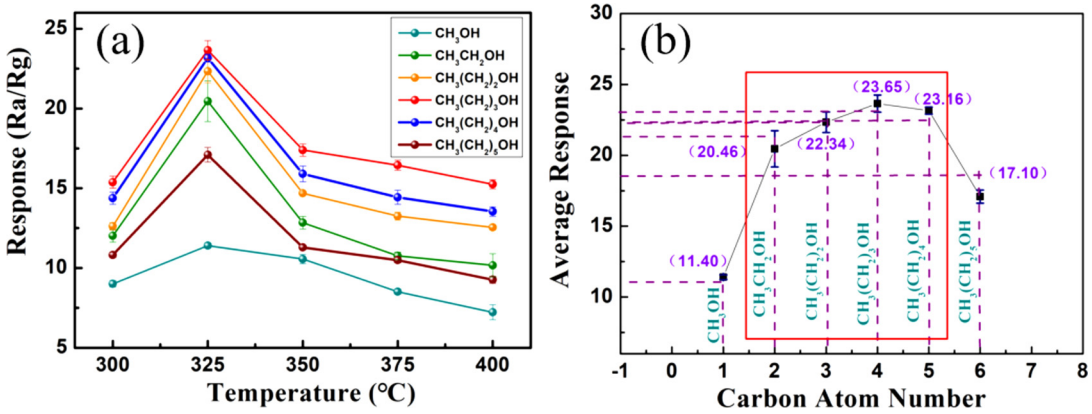

Fig. 5. (a) Response variations vs different operating temperatures. (b) Relationship between response and the carbon atom number at 325 °C. Humidity of the test environment: 30-50 RH %.

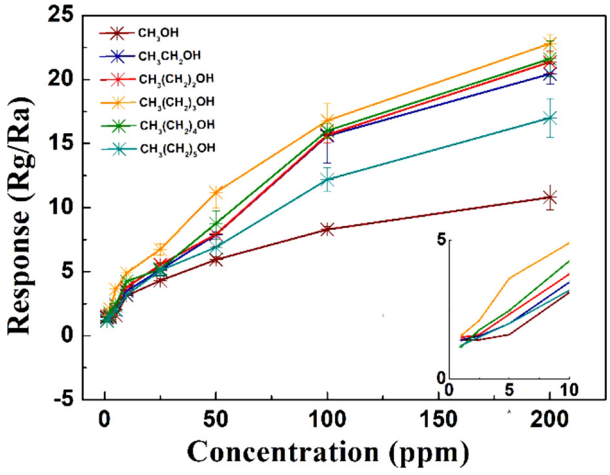

Fig. 6. Response curves to methanol, ethanol, n-propanol, n-butanol, n-pentanol, n-hexanol with different concentrations at 325 °C. Humidity of the test environment: 30-50 RH %.

deduce that the increasing gas viscosity might be the dominant factor that limits he diffusion of the target gas during the recovery process. Gas sensor based on sea cucumber-like nanostructures realize the fast detection to methanol, ethanol, n-propanol, n-butanol, n-pentanol, n-hexanol, which is important for the fabrication of advanced gas sensors.

In practical application, the impact of humidity on sensing performance cannot be neglected. Hence, the responses to various gases with 200 ppm concentration under 25%, 50%, 75% and 95% relative humidity were measured at the optimal operating temperature and shown in Fig. 8(a). From 25 RH% to 50 RH%, the gas responses change slightly. It is considered that the operating temperature of 325 °C could evaporate the water molecules on the material surface. The impact of humidity could be ignored below 50 RH%. However, there is a clear downward trend in gas responses beyond 50 RH%. The change of baseline resistance is responsible to the gas response under the high humidity environment. The variation of baseline resistance with relative humidity is shown in Fig. 8(b). The resistance value decreases with the increase of the relative humidity, this could be explained by the reaction on the material surface between pre-adsorbed O^- and water [49–51]: $H_2O + O- = 2OH + e-$. Terminal hydroxyl groups formed and one electron released to the conduction band by this reaction. The consumption of O^- reduced the available O^- that can participate in the reaction with target gas. Consequently, the response of the sensor is compromised over 50 RH%.

Stability measurement was executed during 20 days, the testing environment was under a relative humidity of 30-50 % at 23-25 °C. The result is shown in Fig. 8(c). The response to methanol maintained around 11. Curve drift appears for the other 5 gases, but the responses are still around 22 for ethanol, n-propanol, n-butanol, n-pentanol as marked by the pink dotted line.

Except the detection of alcohols, responses towards various VOCs including acetaldehyde, acetic acid, isopropanol, ethylene glycol, benzyl alcohol were investigated with 200 ppm concentration for testing the selectivity. The testing environment was under a relative humidity of 30-50 % at 23-25 °C. These gases involved the molecules with functional groups of C = O (acetaldehyde), O = C-OH (acetic acid), isomer of n-propanol (isopropanol), two -OH groups (ethylene glycol), alcohols with benzene ring (benzyl alcohol). The graph of the selectivity results is listed in Fig. 8(d). We speculate that for alcohols detection, the gas response is greatly affected by the -OH number and the -OH position in the molecular chain. For instance, the response to CH_3CH_2OH is 20.5, which is 10 times higher than the response to CH_2OHCH_2OH (response = 2.1). This shows that the -OH number interferes the response of the sensor. Another example, the response of the sensor to $CH_3CH_2CH_2OH$ is 22,3, which is 5 times higher than the response to $CH_3CHOHCH_3$ (response = 4.2). This shows that the -OH position interferes the response of the sensor.

Besides -OH, the sensor is also found to be sensitive to the gases with C = O functional group, such as acetone, formaldehyde, acetaldehyde. While, the sensor shows lowest response to acetic acid, which possesses O = C-OH functional group. Based on these results, we speculate that when detecting VOCs, the type of functional group is critical. The sensitivities of the sensor to functional groups are: -OH > C = O > O = C-OH. The selectivity is affected by the combination of functional group types, functional group number, functional group positions, and molecular chain styles (eg: even with one -OH, the response to benzyl alcohol is only 2). The sensing material is only sensitive to the straight-chain molecules with one -OH functional group at the end of the chain. The selectivity of the sensor demonstrates that the sea cucumber sensing material is especially sensitive and selective to certain kind of alcohols.

Literatures about gas sensors based on various materials are listed in Table1 [52–59]. The survey shows that there is almost no literature reports the sensing performance to n-pentanol and n-hexanol. Compared with the reported literatures, the sensor fabricated here exhibit superior sensing performance, which has potential application in alcohols detection area.

3.3. Gas sensing mechanism

The most widely accepted gas sensing mechanism for n-type oxide semiconductor materials is the resistance change caused by the reaction between adsorbed oxygen and the target gas on the surface of sensing

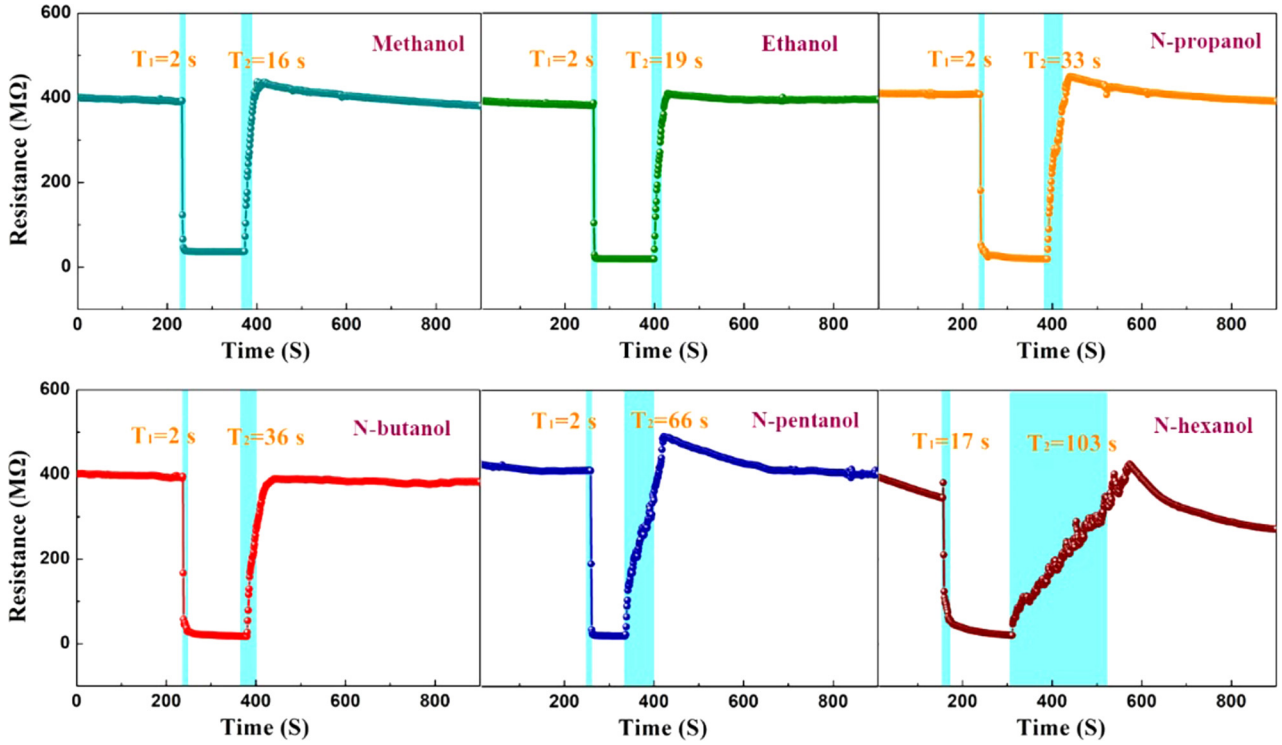

Fig. 7. Real-time resistance curves to 200 ppm of methanol, ethanol, n-propanol, n-butanol, n-pentanol, n-hexanol at 325 °C. Humidity of the test environment: 30-50 RH %.

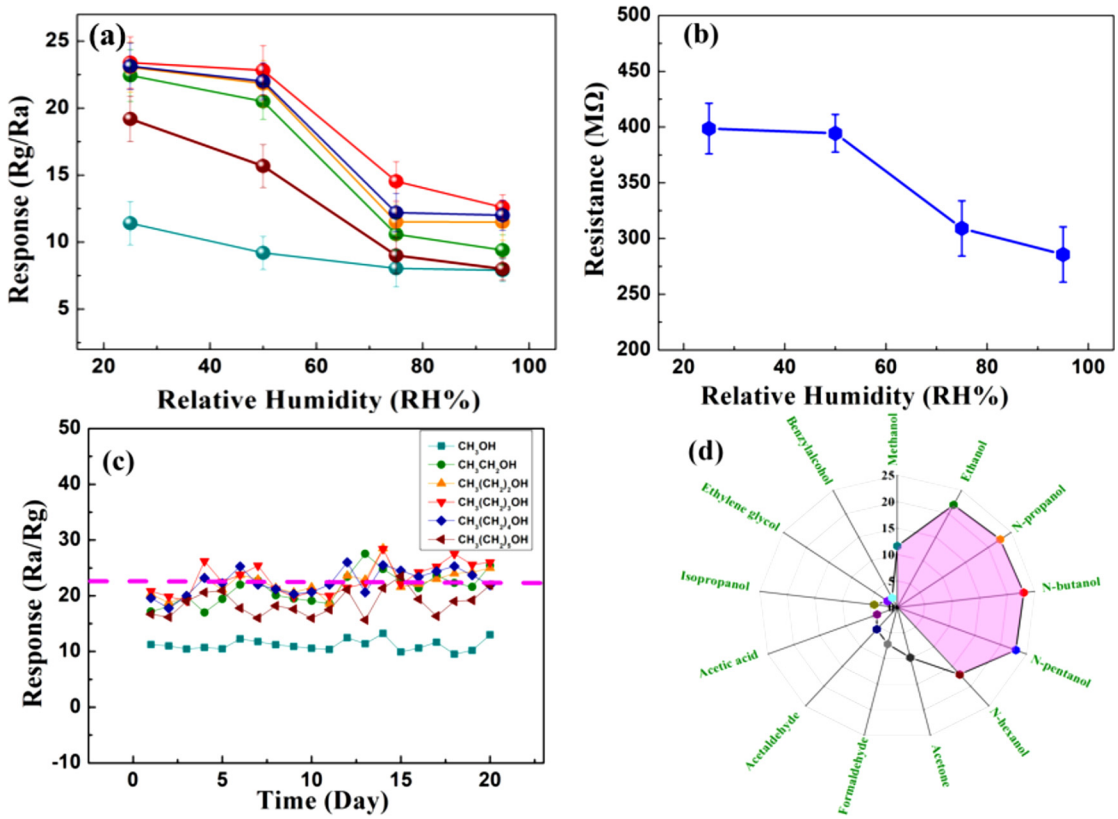

Fig. 8. Relationship between humidity and (a) responses to 200 ppm of methanol, ethanol, n-propanol, n-butanol, n-pentanol, n-hexanol at 325 °C, (b) resistance in air. (c) Sensor stability during 20 days. Humidity of the test environment: 30-50RH %. (d) Responses to other gases with concentration of 200 ppm at 325 °C. Humidity of the test environment: 30-50RH %.

Table 1
Sensing performance to alcohols in the present study and those reported in the literatures [52–59].

Material	Target gas	Concentration	T (℃)	Response(Ra/Rg or Rg/Ra)	Response/Recovery time (s)	Ref.
NiO hollow microspheres	ethanol	100 ppm	350	1.3	< 60/×	[52]
	n-butanol	100 ppm	350	1.7	×	[52]
$FeVO_4$ nanorods	methanol	200 ppm	270	3	×	[53]
	ethanol	200 ppm	270	3.5	×	[53]
	n-butanol	200 ppm	270	11	48/×	[53]
Coral-like Co_3O_4	methanol	1000 ppm	120	13	42/59	[54]
	ethanol	1000 ppm	120	22	22/125	[54]
	n-butanol	1000 ppm	120	27	42/199	[54]
Flower-like WO_3	methanol	100 ppm	320	7.5	×	[55]
	ethanol	100 ppm	320	7.5	×	[55]
	n-butanol	100 ppm	320	5	×	[55]
NiO hollow nanospheres	methanol	800 ppm	240	2.5	×	[56]
	ethanol	800 ppm	240	3	×	[56]
	n-butanol	800 ppm	240	7.2	×	[56]
PtO_2-CuO polyhedron	methanol	100 ppm	180	5.6	×	[57]
	ethanol	100 ppm	180	5.7	×	[57]
	n-butanol	100 ppm	180	11.5	2.4/5.1	[57]
Au-ZnS spheres	ethanol	100 ppm	260	1.98	×	[58]
	n-propanol	100 ppm	260	1.9	×	[58]
	n-butanol	100 ppm	260	1.89	×	[58]
CuO nanowire	methanol	100 ppm	190	2.6	×	[59]
	ethanol	100 ppm	190	4.4	×	[59]
	n-propanol	100 ppm	190	6.2	1.2/6.6	[59]
Indium tungsten oxide	methanol	200 ppm	325	11.6	2/16	This work
	ethanol	200 ppm	325	21.9	2/19	This work
	n-propanol	200 ppm	325	22.6	2/33	This work
	n-butanol	200 ppm	325	23	2/36	This work
	n-pentanol	200 ppm	325	22.9	2/66	This work
	n-hexanol	200 ppm	325	17	17/103	This work

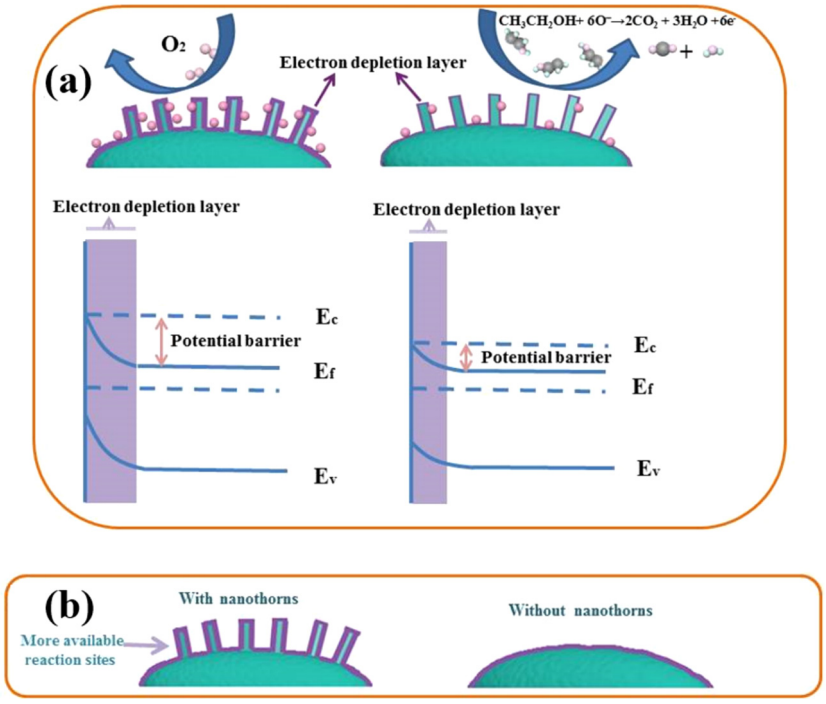

Fig. 9. (a) Illustration of reaction process, (b) schematic diagram of the nanostructures with and without nanothorns.

material [60–61]. According to the sensing behavior of the sea-cucumber nanostructures (resistance decreases when exposed to reducing gas), it is believed that the nanostructures belong to n-type sensing material. The sensing process conforms to the n-type semiconductor sensitive mechanism. In ambient air, the atmospheric oxygen adsorbed on the surface of the material and captured electrons from the conduction band of the material. The transportation of electrons from sensing material to oxygen induced surface negative charge layer formed and determined an upwards band bending. The electron depletion layer contributed to the creation of potential barrier between the adjacent nanograins, resulting the increasing of electrical resistance. The schematic diagram of this process is presented in Fig. 9(a). The ionization process has been investigated by many literatures before [62–64]:

$$O_2\ (g) \rightarrow O_2\ (ads) \quad (1)$$

$$O_2\ (ads) + e^- \rightarrow O_2^-\ (ads)\ (T < 150\ ^\circ C) \quad (2)$$

$$O_2^-\ (ads) + e^- \rightarrow 2O^-\ (ads)\ (150\ ^\circ C < T < 400\ ^\circ C) \quad (3)$$

$$O_2^-\ (ads) + e^- \rightarrow 2O^{2-}\ (ads)\ (T > 400\ ^\circ C) \quad (4)$$

In Fig. 9(a), we take detecting ethanol as an example. When the ethanol gases are introduced in, the gas molecules adsorb on the surface of the material to react with the adsorbed oxygen species. CO_2 and H_2O are released into the air atmosphere as the products of the reaction. The thickness of the depletion layer decreases owing to the removal of the electrons from the oxygen ion to the conduction band. The concentration of the electrons increases and the height of the potential decreases, resulting the decrease of the sensor resistance [64].

According to the previous literatures, the reactions happen between adsorbed oxygen and methanol, ethanol, n-propanol, n-butanol and generate CO_2 and H_2O [65–72]. As no literature has reported the detection of n-pentanol and n-hexanol, it is speculated that reactions for n-pentanol and n-hexanol are similar with that of methanol, ethanol, n-propanol and n-butanol. The reaction processes are described from Eq. 5 to Eq. 10 [65–72],

$$CH_3OH + 3O^- \rightarrow CO_2 + 2H_2O + 3e^- \quad (5)$$

$$CH_3CH_2OH + 6O^- \rightarrow 2CO_2 + 3H_2O + 6e^- \quad (6)$$

$$CH_3(CH_2)_2OH + 9O^- \rightarrow 3CO_2 + 4H_2O + 9e^- \quad (7)$$

$$CH_3(CH_2)_3OH + 12O^- \rightarrow 4CO_2 + 5H_2O + 12e^- \quad (8)$$

$$CH_3(CH_2)_4OH + 15O^- \rightarrow 5CO_2 + 6H_2O + 15e^- \quad (9)$$

$$CH_3(CH_2)_5OH + 18O^- \rightarrow 6CO_2 + 7H_2O + 18e^- \quad (10)$$

The excellent sensing performance of the gas sensor to alcohols could be attributed to the following reasons. I: the special nanostructures of the sensing material. The nanothorns distributed on the nanoellipsoids provide more available sites for the adsorption of oxygen molecules (Fig. 9(b)). As a result, the utilization of sensing body increases and more effective reactions take place on the material surface. As reported by Lee [4], the aggregation of nanoparticles destroys the porous structure and hampers the diffusion of analyte gas toward the inner part of the secondary particles. The TEM result shown in Fig. 2(F) proves that the sea-cucumber nanostructures loosely connect with each other owing to the existence of the nanothorns, providing evidence for the advantage of the nanothorns: tight packing can be avoided compared with the solid structures. This advantage leads to more effective gas diffusions and thus higher response of the sensor. II: chemical components of the material. As reported in many literatures [73–74], the sensing materials with non-stoichiometric ratio always exhibit high response. For ternary semiconductor, the presence of two cations with different atomic radii makes the bond energies weaker compared with binary semiconductor, consequently, it is easier to attract electrons from conduction band. More oxygen ions are formed to enhance the sensitivity of the sensor. III. The CAN and viscosity of the target gas. As discussed above, the sensor is mainly sensitive to certain kind of alcohols. The CAN and viscosity of the target gas affect the response of the sensor together. While, it is still a challenge to figure out the reason that the sensing material is more sensitive to -OH functional group than to others (C = O, COOH, etc.).

4. Conclusions

In this paper, novel sea cucumber-like nanostructures were successfully synthesized for the first time by one-step solvothermal method. The reagents concentration and volume ratio of alcohols to deionized were the key factors to determine the growth of nanothorns onto the nanoellipsoid. The sensor based on the sea cucumber-like nanostructures showed excellent sensing performance to methanol, ethanol, n-propanol, n-butanol, n-pentanol, n-hexanol, especially to ethanol, n-propanol, n-butanol, n-pentanol. It was firstly found the sensor exhibited superior sensing characteristics to straight-chain gas molecules with -OH functional group at the end of the chain. In other words, the sensor realized the detection of gases with common characteristics, which was never reported elsewhere as far as we know. It was speculated the special nanostructure, the chemical components of the material, the CAN and viscosity of the target gas were responsible to the high sensing performance to alcohols. The short response time (2 s, 2 s, 2 s, 2 s, 2 s and 17 s) indicated the sensor were capable of fast detection. All the investigations in this paper provided potential applications in the fast detection of alcohols. Moreover, it inspired the research on gas sensors for a certain type of gas with specific functional group.

CRediT authorship contribution statement

Chong Wang: Conceptualization, Methodology, Software, Investigation, Writing - original draft. **Yiqun Zhang:** Visualization, Investigation. **Xiaoying Sun:** Supervision, Project administration. **Yanfeng Sun:** Software, Validation. **Fangmeng Liu:** Investigation. **Xu Yan:** Funding acquisition. **Chenguang Wang:** Software. **Peng Sun:** Data curation. **Geyu Lu:** Writing- review & editing.

Declaration of Competing Interest

The authors declare that they have no known competing financial interests or personal relationships that could have appeared to influence the work reported in this paper.

Acknowledgements

This work is supported by China Postdoctoral Science Foundation (801191050420, 801191060420, 801201030420). Science and Technology Department of Jilin Province (No. 20190103054JH).

Appendix A. Supplementary data

Supplementary material related to this article can be found, in the online version, at doi:https://doi.org/10.1016/j.snb.2020.128158.

References

[1] M.R. Alenezi, S.J. Henley, N.G. Emerson, S.R. Silva, From 1D and 2D ZnO nanostructures to 3D hierarchical structures with enhanced gas sensing properties, Nanoscale 6 (2014) 235–247.
[2] A. Perego, G. Giuffredi, P. Mazzolini, M. Colombo, R. Brescia, M. Prato, D.C. Sabarirajan, I.V. Zenyuk, F. Bossola, V.D. Santo, A. Casalegno, F.D. Fonzo, Hierarchical TiN nanostructured thin film electrode for highly stable PEM fuel cells, ACS Appl. Energy Mater. 2 (2019) 1911–1922.
[3] J. Chen, M. Wang, J. Han, R. Guo, TiO_2 nanosheet/NiO nanorod hierarchical nanostructures: p–n heterojunctions towards efficient photocatalysis, J. Colloid Interface Sci. 562 (2020) 313–321.
[4] J.-H. Lee, Gas sensors using hierarchical and hollow oxide nanostructures: Overview, Sens. Actuators B 1 (2009) 319–336.
[5] G. Qi, S. Zhao, Z. Yuan, From function-guided assembly of a lotus leaf-like ZnO nanostructure to a formaldehyde gas-sensing application, Sens. Actuators B 184 (2013) 143–149.
[6] W. Guo, T. Liu, R. Sun, Y. Chen, W. Zeng, Z. Wang, Hollow, porous, and yttrium functionalized ZnO nanospheres with enhanced gas-sensing performances, Sens. Actuators B 178 (2013) 53–62.
[7] C. Wang, X. Li, C. Feng, Y. Sun, G. Lu, Nanosheets assembled hierarchical flower-like WO_3 nanostructures: Synthesis, characterization, and their gas sensing properties, Sens. Actuators B 210 (2015) 75–81.
[8] D.F. Zhang, L.D. Sun, J.L. Yin, C.H. Yan, Low-temperature fabrication of highly crystalline SnO_2 nanorods, Adv. Mater. 12 (2003) 1022–1025.
[9] E. Comini, G. Faglia, G. Sberveglieri, Z. Pan, Z.L. Wang, Stable and highly sensitive gas sensors based on semiconducting oxide nanobelts, Appl. Phys. Lett. 81 (2002) 1869–1871.
[10] L. Wang, Y. Kang, X. Liu, S. Zhang, W. Huang, S. Wang, ZnO nanorod gas sensor for ethanol detection, Sens. Actuators B 1 (2012) 237–243.
[11] Z.Y. Zhang, X.H. Li, C.H. Wang, L.M. Wei, Y.C. Liu, C.L. Shao, ZnO hollow nanofibers: fabrication from facile single capillary electrospinning and applications in

gas sensors, J. Phys. Chem. C 113 (2009) 19397–19403.
[12] H. Xia, Y. Wang, F. Kong, S. Wang, B. Zhu, X. Guo, J. Zhang, Y. Wang, S. Wu, Au-doped WO_3-based sensor for NO_2 detection at low operating temperature, Sens. Actuators B 1 (2008) 133–139.
[13] H. Najafi-Ashtiani, The effect of different surface morphologies on WO_3 and WO_3-Au gas-sensors performance, J. Mater. Sci.: Mater. in Electron. 13 (2019) 12224–12233.
[14] D.H. Zhang, Z.Q. Liu, C. Li, T. Tang, X.L. Liu, S. Han, B. Lei, C.W. Zhou, Detection of NO_2 down to ppb levels using individual and multiple In_2O_3 nanowire devices, Nano Lett. 4 (2004) 1919–1924.
[15] B.X. Li, Y. Xie, M. Jing, G.X. Rong, Y.C. Tang, G.Z. Zhang, In_2O_3 hollow microspheres synthesis from designed $In(OH)_3$ precursors and applications in gas sensors and photocatalysis, Langmuir 22 (2006) 9380–9385.
[16] X. Deng, L. Zhang, J. Guo, Q. Chen, J. Ma, ZnO enhanced NiO-based gas sensors towards ethanol, Mater. Res. Bull. 90 (2017) 170–174.
[17] S.M. Majhi, G.K. Naik, H.-J. Lee, H.-G. Song, C.-R. Lee, I.-H. Lee, Y.-T. Yu, Au@NiO core-shell nanoparticles as a p-type gas sensor: Novel synthesis, characterization, and their gas sensing properties with sensing mechanism, Sens. Actuators B 268 (2018) 223–231.
[18] Y. Li, J. Liang, Z. Tao, J. Chen, CuO particles and plates: Synthesis and gas-sensor application, Mater. Res. Bull. 43 (2008) 2380–2385.
[19] H.J. Park, N.-J. Choi, H. Kang, M.Y. Jung, J.W. Park, K.H. Park, D.-S. Lee, A ppb-level formaldehyde gas sensor based on CuO nanocubes prepared using a polyol process, Sens. Actuators B 203 (2014) 282–288.
[20] T.T. Xu, X.F. Zhang, X. Dong, Z.P. Deng, L.H. Huo, S. Gao, Enhanced H_2S gas-sensing performance of Zn_2SnO_4 hierarchical quasi-microspheres constructed from nanosheets and octahedra, J. Hazard. Mater. 361 (2019) 49–55.
[21] Y. Li, N. Luo, G. Sun, B. Zhang, H. Jin, L. Lin, H. Bala, J. Cao, Z. Zhang, Y. Wang, Synthesis of porous nanosheets-assembled $ZnO/ZnCo_2O_4$ hierarchical structure for TEA detection, Sens. Actuators B 287 (2019) 199–208.
[22] O. Lupan, V. Cretu, V. Postica, O. Polonskyi, N. Ababii, F. Schütt, V. Kaidas, F. Faupel, R. Adelung, Non-planar nanoscale p-p heterojunctions formation in ZnxCu1-xOy nanocrystals by mixed phases for enhanced sensors, Sens. Actuators B 230 (2016) 832–843.
[23] A. Mirzaei, S.G. Leonardi, G. Neri, Detection of hazardous volatile organic compounds (VOCs) by metal oxide nanostructures-based gas sensors: A review, Ceram. Int. 14 (2016) 15119–15141.
[24] D.J. Guo, J.M. You, Highly catalytic activity of Pt electrocatalyst supported on sulphated SnO_2/multi-walled carbon nanotube composites for methanol electro-oxidation, J. Power Sources 198 (2012) 127–131.
[25] L.O. Peres, R.W.C. Li, E.Y. Yamauchi, R. Lippi, J. Gruber, Conductive polymer gas sensor for quantitative detection of methanol in brazilian dugar-cane dpirit, Food Chem. 130 (2012) 1105–1107.
[26] A.K. Nayak, R. Ghosh, S. Santra, P.K. Guha, D. Pradhan, Hierarchical nanostructured WO_3-SnO2 for selective sensing of volatile organic compounds, Nanoscale 7 (2015) 12460–12473.
[27] Z. Guo, Z. Jiang, X. Chen, B. Sun, M. Li, J. Liu, X. Huang, Novel cocoon-like Au/La_2O_3 nanomaterials: synthesis and their ultra-enhanced cataluminescence performance to volatile organic compounds, J. Mater. Chem. 21 (2011) 1874–1879.
[28] A.S. Zoolfakar, M.Z. Ahmad, R.A. Rani, J.Z. Ou, S. Balendhran, S. Zhuiykov, K. Latham, W. Wlodarski, K. Kalantar-zadeh, Nanostructured copper oxides as ethanol vapour sensors, Sens. Actuators B 185 (2013) 620–627.
[29] O. Lupan, V. Cretu, V. Postica, N. Ababii, O. Polonskyi, V. Kaidas, F. Schütt, Y.K. Mishra, E. Monaico, I. Tiginyanu, V. Sontea, T. Strunskus, F. Faupel, R. Adelung, Enhanced ethanol vapour sensing performances of copper oxide nanocrystals with mixed phases, Sens. Actuators B 224 (2016) 434–448.
[30] M. Righettoni, A. Tricoli, S.E. Pratsinis, Si: WO_3 sensors for highly selective detection of acetone for easy diagnosis of diabetes by breath analysis, Anal. Chem. 82 (2010) 3581–3587.
[31] X. Jia, C. Cheng, S. Yu, J. Yang, Y. Li, H. Song, Preparation and enhanced acetone sensing properties of flower-like α-Fe_2O_3/multi-walled carbon nanotube nanocomposites, Sens. Actuators B 300 (2019) 127012.
[32] J.A. Dirksen, K. Duval, T.A. Ring, NiO thin-film formaldehyde gas sensor, Sens. Actuators B 80 (2001) 106–115.
[33] R. Zhang, S.Y. Ma, Q.X. Zhang, K.M. Zhu, Y. Tie, S.T. Pei, B.J. Wang, J.L. Zhang, Highly sensitive formaldehyde gas sensors based on Ag doped Zn_2SnO_4/SnO_2 hollow nanospheres, Mater. Lett. 254 (2019) 178–181.
[34] Y. Zeng, T. Zhang, L. Wang, M. Kang, H. Fan, R. Wang, Y. He, Enhanced toluene sensing characteristics of TiO2-doped flowerlike ZnO nanostructures, Sens. Actuators B 1 (2009) 73–78.
[35] Y. Zhang, C. Jia, Q. Wang, Q. Kong, G. Chen, H. Guan, C. Dong, MOFs-derived porous $NiFe_2O_4$ nano-octahedrons with hollow interiors for an excellent toluene gas sensor, Nanomaterials 9 (2019) 1059.
[36] T.-H. Kim, S.-Y. Jeong, Y.K. Moon, J.-H. Lee, Dual-mode gas sensor for ultra-sensitive and highly selective detection of xylene and toluene using Nb-doped NiO hollow spheres, Sens. Actuators B 301 (2019) 127140.
[37] J.-H. Kim, J.-H. Lee, Y. Park, J.-Y. Kim, A. Mirzaei, H.W. Kim, S.S. Kim, Toluene- and benzene-selective gas sensors based on Pt- and Pd-functionalized ZnO nanowires in self-heating mode, Sens. Actuators B 294 (2019) 78–88.
[38] C. Wang, R. Sun, X. Li, Y. Sun, P. Sun, F. Liu, G. Lu, Hierarchical flower-like WO_3 nanostructures and their gas sensing properties, Sens. Actuators B 204 (2014) 224–230.
[39] J. Mu, B. Chen, M.Y. Zhang, Z. Guo, P. Zhang, Z. Zhang, Y. Sun, C. Shao, Y. Liu, Enhancement of the visible-light photocatalytic activity of In_2O_3-TiO_2 nanofiber heteroarchitectures, ACS Appl. Mater. Interfaces 4 (2012) 424–430.
[40] R.K. Chava, S.Y. Oh, Y.T. Yu, Enhanced H_2 gas sensing properties of Au@In_2O_3 core-shell hybrid metal-semiconductor heteronanostructures, CrystEngComm 18 (2016) 3655–3666.
[41] J.C. Dupin, D. Gonbeau, P. Vinatier, A. Levasseur, Systematic XPS studies of metal oxides, hydroxides and peroxides, Phys. Chem. Chem. Phys. 2 (2000) 1319–1324.
[42] L.Q. Zhang, Z.Z. Ye, J.G. Lu, B. Lu, Y.Z. Zhang, L.P. Zhu, J. Zhang, D. Yang, K.W. Wu, J. Huang, Influence of p-type and n-type dopants on the magnetic properties of ZnCuO based diluted magnetic semiconductor thin films, J. Phys. D: Appl. Phys. 43 (2010) 015001.
[43] J. Liu, M. Dai, T. Wang, P. Sun, X. Liang, G. Lu, K. Shimanoe, N. Yamazoe, Enhanced gas sensing properties of SnO_2 hollow spheres decorated with CeO_2 nanoparticles heterostructurecomposite materials, ACS Appl. Mater. Interfaces 8 (2016) 2–10.
[44] C. Wang, X. Kou, N. Xie, L. Guo, Y. Sun, X. Chuai, J. Ma, P. Sun, Y. Wang, G. Lu, Detection of methanol with fast response by monodispersed indium tungsten oxide ellipsoidal nanospheres, ACS Sens. 5 (2017) 648–654.
[45] X. Zhou, J. Liu, C. Wang, P. Sun, X. Hu, X. Li, K. Shimanoe, N. Yamazoe, G. Lu, Highly sensitive acetone gas sensor based on porous $ZnFe_2O_4$ nanospheres, Sens. Actuators B 206 (2015) 577–583.
[46] X.Q. An, J.C. Yu, Y. Wang, Y.M. Hu, X.L. Yu, G.J. Zhang, WO_3 nanorods/graphene nanocomposites for high-efficiency visible-light-driven photocatalysis and NO_2 gas sensing, J. Mater. Chem. 22 (2012) 8525–8531.
[47] B. Ruhland, Th. Becker, G. Müller, Gas-kinetic interactions of nitrous oxides with SnO_2 surface, Sens. Actuators B 50 (1998) 85–94.
[48] A.P. Lee, B.J. Reedy, Temperature modulation in semiconductor gas sensing, Sens. Actuators B 60 (1999) 35–42.
[49] C. Su, L. Zhang, Y.T. Han, C. Ren, X.W. Chen, J. Hu, M. Zeng, N.T. Hu, Y.J. Su, Z.H. Zhou, Z. Yang, Controllable synthesis of crescent-shaped porous NiO nanoplates for conductometric ethanol gas sensors, Sens. Actuators B 296 (2019) 126642.
[50] M. Hübner, C.E. Simion, A. Tomescu-Stanoiu, S. Pokhrel, N. Bârsan, U. Weimar, Influence of humidity on CO sensing with p-type CuO thick film gas sensors, Sens. Actuators B 153 (2011) 347–353.
[51] D. Koziej, N. Baˆrsan, U. Weimar, J. Szuber, K. Shimanoe, N. Yamazoe, Water–oxygen interplay on tin dioxide surface: Implication on gas sensing, Sens. Actuators B 410 (2005) 321–323.
[52] G. Zhu, C. Xi, H. Xu, D. Zheng, Y. Liu, X. Xu, X. Shen, Hierarchical NiO hollow microspheres assembled from nanosheet-stacked nanoparticles and their application in a gas sensor, RSC Adv. 2 (2012) 4236–4241.
[53] Y.V. Kaneti, Z. Zhang, J. Yue, X. Jiang, A. Yu, Porous $FeVO_4$ nanorods: synthesis, characterization, and gas-sensing properties toward volatile organic compounds, J. Nanopart. Res. 15 (2013) 1948.
[54] S. Deng, N. Chen, D. Deng, Y. Li, X. Xing, Y. Wang, Meso- and macroporous coral-like Co_3O_4 for VOCs gas sensor, Ceram. Int. 9 (2015) 11004–11012.
[55] J. Huang, X. Xu, C. Gu, M. Yang, M. Yang, J. Liu, Large-scale synthesis of hydrated tungsten oxide 3D architectures by a simple chemical solution route and their gas-sensing properties, J. Mater. Chem. 21 (2011) 3283–13289.
[56] S. Chu, C. Yang, X. Su, Synthesis of NiO hollow nanospheres via Kirkendall effect and their enhanced gas sensing performance, Appl. Surf. Sci. 492 (2019) 82–88.
[57] B. Yang, J. Liu, H. Qin, Q. Liu, X. Jing, H. Zhang, R. Li, G. Huang, J. Wang, PtO_2-nanoparticles functionalized CuO polyhedrons for n-butanol gas sensor application, Ceram. Int. 9 (2018) 10426–10432.
[58] L. Zhang, R. Dong, Z. Zhu, S. Wang, Au nanoparticles decorated ZnS hollow spheres for highly improved gas sensor performances, Sens. Actuators B 245 (2017) 112–121.
[59] J. Tan, M. Dun, L. Li, J. Zhao, X. Li, Y. Hu, G. Huang, W. Tan, X. Huang, Self-template derived CuO nanowires assembled microspheres and its gas sensing properties, Sens. Actuators B 252 (2017) 1–8.
[60] S. Lenaerts, J. Roggen, G. Maes, FT-IR characterization of tin dioxide gas sensor materials under working conditions, Spectrochim. Acta, Part A 51 (1995) 883–894.
[61] N. Yamazoe, J. Fuchigami, M. Kishikawa, T. Seiyama, Interactions of tin oxide surface with O_2, H_2O AND H_2, Surf. Sci. 86 (1979) 335–344.
[62] N. Barsan, J. Rebholz, U. Weimar, Conduction mechanism switch for SnO_2 based sensors during operation in application relevant conditions; implications for modeling of sensing, Sens. Actuators B 207 (2015) 455–459.
[63] F.E. Annanouch, Z. Haddi, S. Vallejos, P. Umek, P. Guttmann, C. Bittencourt, E. Llobet, Aerosol-assisted CVD-grown WO_3 nanoneedles decorated with copper oxide nanoparticles for the selective and humidity-resilient detection of H_2S, ACS Appl. Mater. Interfaces 7 (2015) 6842–6851.
[64] Y. Qu, H. Wang, H. Chen, M. Han, Z. Lin, Synthesis, characterization and sensing properties of mesoporous C/SnO_2 nanocomposite, Sens. Actuators B 228 (2016) 595–604.
[65] A. Saaedi, P. Shabani, R. Yousefi, High performance of methanol gas sensing of ZnO/PAni nanocomposites synthesized under different magnetic field, J. Alloys Compd. 802 (2019) 335–344.
[66] S. Taha, S. Begum, V.N. Narwade, D.I. Halge, J.W. Dadge, M.P. Mahabole, R.S. Khairnar, K.A. Bogle, Development of alcohol sensor using TiO_2-Hydroxyapatite nano-composites, Mater. Chem. and Phys. 240 (2020) 122228.
[67] H.N. TTD.Nguyen, M.J. Choi, D.V. Ahemad, I.H. Dao, Y.T. Lee, Yu, Hydrothermal synthesis of In_2O_3 nanocubes for highly responsive and selective ethanol gas sensing, J. Alloys Compd. 820 (2020) 153133.
[68] Z. Tang, X. Deng, Y. Zhang, X. Guo, J. Yang, C. Zhu, Jie fan, Y. Shi, B. Qing, F. Fan, MoO_3 nanoflakes coupled reduced graphene oxide with enhanced ethanol sensing performance and mechanism, Sens. Actuators B 297 (2019) 126730.
[69] K.T. Alali, Z. Lu, H. Zhang, J. Liu, Q. Liu, R. Li, K. Aljebawi, J. Wang, P-p heterojunction $CuO/CuCo_2O_4$ nanotubes synthesized via electrospinning technology for detecting n-propanol gas at room temperature, Inorg. Chem. Front. 4 (2017) 1219.
[70] C. Dong, X. Xing, N. Chen, X. Liu, Y. Wang, Biomorphic synthesis of hollow CuO

fibers for low-ppm-level n-propanol detection via a facile solution combustion method, Sens. Actuators B 230 (2016) 1–8.
[71] J. Bai, Y. Li, Y. Liu, H. Wang, F. Liu, F. Liu, P. Sun, X. Yan, G. Lu, $Au_{39}Rh_{61}$ alloy nanocrystal-decorated $W_{18}O_{49}$ for enhanced detection of n-butanol, ACS Sens. 4 (2019) 2662–2670.
[72] W. Liu, X. Zhang, Z. Wang, R. Wang, C. Chen, C. Dong, Nanoparticles assembled $CdIn_2O_4$ spheres with high sensing properties towards n-butanol, Nanomater. 9 (2019) 1714.
[73] L. Zhu, Y. Wang, D. Zhang, C. Li, D. Sun, S. Wen, Y. Chen, S. Ruan, Gas Sensors based on metal sulfide $Zn_{(1-x)}Cd_{(x)}S$ nanowires with excellent performance, ACS Appl. Mater. Interfaces 37 (2015) 20793–20800.
[74] Y. Chen, L. Zhu, C. Feng, J. Liu, C. Li, S. Wen, S. Ruan, Low temperature operating $In_{2-x}Ni_xO_3$ sensors with high response and good selectivity for NO_2 gas, J. Alloys Compd. 581 (2013) 653–658.

Chong Wang obtained her PhD from Jilin University of China in 2018. Now, she is a postdoctor majored in information and communication engineering. Her main research is about chemical gas sensor based on functional materials and the practical application for communication.

Yiqun Zhang received her PhD degree in 2019 from College of Electronic Science and Engineering, Jilin University, China. Now she is a postdoctor in Jilin University. Her current research mainly focus on the development of gas sensor and the application for communication.

Xiaoying Sun received the B.S. and M.S. degrees from Jilin University, Jilin, China, in 1991 and 1994, respectively, and the Ph.D. degree in communication and information systems from Jilin University. He is currently a Professor with the Laboratory of Signals Detection and Processing, Jilin University, where he is also a Professor, a Changbai Mountain Scholar, and the Dean of the Communication Engineering College. His current research interests include array signal processing, wireless localization, and human–computer interaction.

Yanfeng Sun obtained his PhD from Jilin University of China in 2007. Presently, he is working as professor in Electronics Science and Engineering department of Jilin University. His current research interests are nanoscience and gas sensors.

Fangmeng Liu received his B.S. degree in 2009, Liaocheng University and M.S. degree in2012 from Northeast Forestry University in china. In 2016, he received Ph.D. degree in Jilin University. Now, he is working in Jilin University.

Xu Yan received his M.S. degree in 2013 from Nanjing Agricultural University. He joined the group of Prof. Xingguang Su at Jilin Unibersity and received his Ph.D. degree in June 2017. Since then, he did postdoctoral work with Prof. Guyu Lu and Prof. Junqiu Liu. Currently, his research interests mainly focus on the development of the functional nanomaterials for chem/bio sensors.

Chenguang Wang received his PhD degree from the College of Chemistry, Jilin University in 2013. He then joined the Institute of Transformative Bio-Molecules, Nagoya University as a postdoctoral fellow. In 2019, he joined the College of Electronic Science and Engineering, Jilin University as a professor. His research interests focus on the design and synthesis of organic fluorescent molecules and their applications in fluorescence bioimaging.

Peng Sun received his MS degree from State Key Laboratory of Superhard Materials, Jilin University, China in 2009. He entered the PhD course in 2010, majored in microelectronics and solid-state electronics. Now, he is engaged in the synthesis and characterization of the semiconducting functional materials and gas sensors.

Geyu Lu received the BS degree in electronic sciences in 1985 and the MS degree in 1988 from Jilin University in China and the Dr Eng degree in 1998 from Kyushu University in Japan. Now he is a professor of Jilin University, China. Now, he is interested in the development of functional materials and chemical sensors